

Short gamma-ray burst jet propagation in binary neutron star merger environments

Andrea Pavan,^{1,2,3}★ Riccardo Ciolfi,^{2,3}† Jay V. Kalinani^{1,3} and Andrea Mignone⁴

¹*Dipartimento di Fisica e Astronomia, Università di Padova, Via Francesco Marzolo 8, I-35131 Padova, Italy*

²*INAF, Osservatorio Astronomico di Padova, Vicolo dell'Osservatorio 5, I-35122 Padova, Italy*

³*INFN, Sezione di Padova, Via Francesco Marzolo 8, I-35131 Padova, Italy*

⁴*Dipartimento di Fisica, Università di Torino, Via Pietro Giuria 1, I-10125 Torino, Italy*

Accepted XXX. Received YYY; in original form ZZZ

ABSTRACT

The multimessenger event GW170817/GRB 170817A confirmed that binary neutron star (BNS) mergers can produce short gamma-ray burst (SGRB) jets. This evidence promoted new investigations on the mechanisms through which a BNS merger remnant can launch such a powerful relativistic outflow and on the propagation of the latter across the surrounding post-merger environment. In particular, great strides have been made in jet propagation models, establishing connections between the initial jet launching conditions, including the incipient jet launching time (with respect to merger) and the injection parameters, and the observable SGRB prompt and afterglow emission. However, present semi-analytical models and numerical simulations (with one notable exception) adopt simple hand-made prescriptions to account for the post-merger environment, lacking a direct association with any specific merging BNS system. Here, we present the first three-dimensional relativistic hydrodynamics simulations of incipient SGRB jets propagating through a post-merger environment that is directly imported from the outcome of a previous general relativistic BNS merger simulation. Our results show that the evolution and final properties of the jet can be largely affected by the anisotropies and the deviations from axisymmetry and homologous expansion characterizing more realistic BNS merger environments. In addition, we find that the inclusion of the gravitational pull from the central compact object, often overlooked, can have a major impact. Finally, we consider different jet launching times referred to the same BNS merger model and discuss the consequences for the ultimate jet properties.

Key words: gamma-ray bursts – stars: jets – neutron star mergers – hydrodynamics – relativistic processes – methods: numerical.

1 INTRODUCTION

The first multimessenger observation of a binary neutron star (BNS) merger in 2017, combining gravitational waves (GWs) with a variety of electromagnetic (EM) signals across the entire spectrum, marked a major milestone in the investigation of these extraordinary astrophysical events (Abbott et al. 2017a,b,c,d; see, e.g., Ciolfi 2020b; Nakar 2020 and refs. therein). Among the numerous discoveries, the coincident detection of the gamma-ray signal GRB 170817A and the following observation of a multiwavelength afterglow confirmed the long-standing hypothesis that BNS mergers can produce relativistic jets and power short gamma-ray bursts (SGRBs) (Abbott et al. 2017d; Goldstein et al. 2017; Hallinan et al. 2017; Savchenko et al. 2017; Troja et al. 2017; Lazzati et al. 2018; Lyman et al. 2018; Mooley et al. 2018a,b; Ghirlanda et al. 2019). Moreover, this SGRB was observed from a viewing angle $\approx 15^\circ - 20^\circ$ away from the main jet propagation axis, offering unprecedented insights into the angular structure of the relativistic outflows associated with SGRBs (Mooley et al. 2018b; Ghirlanda et al. 2019; see, e.g., Ioka & Nakamura 2019 and refs. therein).

Despite this breakthrough discovery, key open questions remain on both the nature of the SGRB central engine (either a massive neutron star or an accreting black hole) and the jet launching mechanism itself. Observational data from GRB 170817A and the accompanying afterglow signals directly probed the properties of the relativistic outflow emerging from the baryon-polluted environment surrounding the merger site, but not the physical conditions of the system at the time the incipient jet was initially launched.

In order to connect the ultimate jet structure and its EM signatures with the properties of the incipient jet (initial opening angle and power, total energy, etc.) and the post-merger environment, including the jet launching time with respect to merger, a growing effort is devoted to model the breakout and propagation of collimated relativistic outflows following BNS mergers. Such an effort, strongly boosted by the observation of GRB 170817A, includes semi-analytical models (e.g., Salafia et al. 2020; Lazzati et al. 2020; Hamidani & Ioka 2021 and refs. therein) as well as two- or three-dimensional (magneto)hydrodynamic simulations in the framework of special or general relativity (e.g., Lazzati et al. 2018; Xie et al. 2018; Kathirgamaraju et al. 2019; Geng et al. 2019; Nathanail et al. 2020; Murguía-Berthier et al. 2021; Urrutia et al. 2021; Nathanail et al. 2021; Gottlieb et al. 2021 and refs. therein).

While the physical description provided by the above modelling

★ E-mail: andrea.pavan.20@phd.unipd.it (AP)

† E-mail: riccardo.ciolfi@inaf.it (RC)

effort is continuously improving, current studies share one important limitation: the density, pressure, and velocity distributions characterizing the surrounding environment at the jet launching time are the result of hand-made prescriptions that should reproduce a typical post-merger system, but have no direct connection with any specific merging BNS.¹

As a first step towards a consistent end-to-end description covering merger, jet launching, and jet propagation, we present here the first three-dimensional (3D) special relativistic hydrodynamic simulations of incipient SGRB jets where the initial conditions of the surrounding environment are directly imported from the outcome of a fully general relativistic BNS merger simulation. We discuss the details of the setup and the adopted prescriptions, along with the results of a number of simulations testing different aspects of our approach. Our findings on a fiducial model reveal the severe limitations of employing hand-made environment initial data as opposed to the outcome of actual BNS merger simulations. Moreover, they demonstrate the importance of including the effects of the gravitational pull from the central object. Referring to the same merging BNS, we vary the time (after merger) at which the jet is launched and show how this affects the final structure and properties of the escaping jet. This work serves mostly as a demonstration of the approach, paving the way for future explorations of the relevant parameter space and the first application to events like GRB 170817A.

The paper is organized as follows. Section 2 presents our setup in terms of numerical methods, initial data, grid structure, boundary conditions, and jet injection properties. Our fiducial model is discussed in Section 3, where we also consider test cases where we remove the contribution of external forces (including gravity) and, in one case, we also substitute the initial surrounding environment with a much simpler matter distribution inspired by prescriptions typically adopted in the literature. In Section 4, we consider a different jet injection time and discuss the impact on the final outcome. Finally, a summary of the work and concluding remarks are given in Section 5.

2 PHYSICAL AND NUMERICAL SETUP

We perform our special relativistic hydrodynamic simulations using the publicly available code PLUTO, version 4.4 (Mignone et al. 2007, 2012). The code provides a multi-physics, multi-algorithm modular environment designed to solve conservative problems in different spatial dimensions and systems of coordinates, especially in presence of strong discontinuities. We carry out our simulations using the HLL Riemann solver, piecewise parabolic reconstruction and 3rd-order Runge Kutta time stepping in 3D spherical coordinates (r, θ, ϕ) . When setting the computational domain in the radial direction, we “excise” the central region up to a radius of $r_{\text{exc}} = 380$ km, i.e. we do not evolve the inner part of the system. A careful choice of the boundary conditions on the corresponding spherical surface allows for angle dependent ingoing and outgoing fluxes according to the combined effects of gravitational pull and radial pressure gradients (see Section 2.2). Moreover, the incipient jet is introduced into the computational domain from the same surface and thus our jet prescription (Section 2.3) refers to its properties at 380 km from the central engine. We also note that general relativistic effects, which are not accounted for in PLUTO, can be safely neglected above 380 km.

The initial setup of our simulations is based on the outcome of a previous general relativistic BNS merger simulation, from which data are imported. The physical and numerical setup of such BNS merger simulation is identical to the one employed in Cioffi (2020a), except that in this case magnetic fields are not present. In particular, the BNS system at hand has the same chirp mass as the one estimated for GW170817 (Abbott et al. 2019), with mass ratio $q \approx 0.9$, and the equation of state (EOS) adopted for neutron star (NS) matter is a piece-wise polytropic approximation of the APR4 EOS (Akmal et al. 1998) as implemented in Endrizzi et al. (2016). The above choices lead to a long-lived supramassive NS as the merger remnant, which would survive the collapse to a black hole (BH) for much longer than the evolution time covered by the simulation, i.e. up to 156 ms after merger. The BNS merger simulation employs a 3D Cartesian grid with 7 refinements levels and finest grid spacing of ≈ 250 m, extending up to ≈ 3400 km along all axes. To save computational resources, we also enforced reflection symmetry across the $z = 0$ equatorial plane. An artificial constant density floor of $\rho^* \approx 6.3 \times 10^4$ g/cm³ is also set in the numerical domain, corresponding to a total mass of $\approx 3.5 \times 10^{-3} M_{\odot}$. We refer the reader to Cioffi et al. (2017, 2019) and Cioffi (2020a) for further details about numerical codes and methods.

In this work, we adopt the paradigm in which a SGRB jet is launched by the accreting BH system resulting from the eventual collapse of the massive NS remnant. While the SGRB central engine is still a matter of debate, this scenario remains the leading one and also finds support in BNS merger simulations (Ruiz et al. 2016; Cioffi 2020a; see, e.g., Cioffi 2020c for a review). For the time being, we assume that the collapse occurs at a chosen time along the massive NS remnant evolution and we use the physical conditions of the system at that time to start our PLUTO simulations. After a short (order ~ 10 ms) transition interval to account for the effects of the forming BH-accretion disk system, we introduce the jet with a given set of properties. This choice allows us to control the parameters of the injection, which is very convenient for a first investigation, and to explore the effects of a different collapse time on an otherwise identical system.²

In the following, we discuss in detail our prescriptions, including data import, grid settings, boundary conditions, treatment of external forces, jet injection, and more.

2.1 Data import and computational grid

Our reference BNS merger simulation leads to a remnant NS of gravitational mass $M_0 \approx 2.596 M_{\odot}$ and follows its evolution up to 156 ms after merger. Along the evolution, we save 3D outputs of rest-mass density, pressure, 3-velocity, and specific internal energy every ≈ 5 ms. For a chosen time at which the remnant NS is assumed to collapse, we import the corresponding data in PLUTO according to the following steps:

- First, data are mapped onto a uniform 3D Cartesian grid using the PostCactus Python package³ and setting the resolution of the new grid to be the same of the BNS merger simulation at 380 km from the origin (i.e. ≈ 8.2 km, sixth refinement level). In this step,

¹ An exception is represented by Nativi et al. (2021), where the environment is set by importing data from a newtonian simulation of neutrino-driven winds produced by a massive neutron star remnant (Perego et al. 2014).

² Importing data from BNS merger simulations directly covering the collapse and the formation of an incipient jet would represent a further crucial step towards a fully consistent end-to-end description and should be the goal of future studies.

³ <https://github.com/wokast/PyCactus>

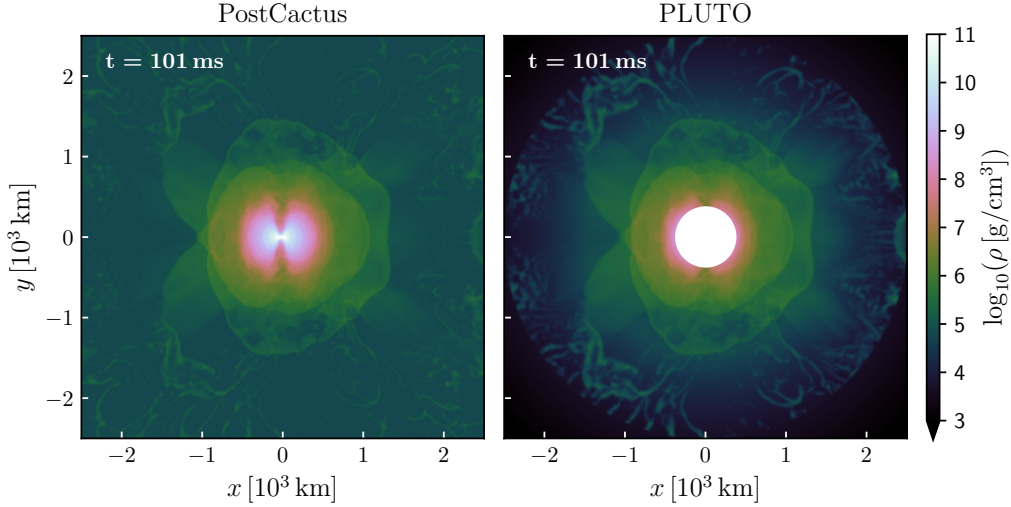


Figure 1. Meridional view of the rest-mass density as obtained by importing data from the reference BNS merger simulation at 101 ms post-merger (see text). The left panel shows the result of the PostCactus interpolation, while the right panel shows the final setup on the PLUTO grid. The white circle of 380 km radius in the right panel corresponds to the excised region (that we do not evolve in PLUTO).

we exploit the equatorial symmetry to obtain the data on the full domain (i.e. for both positive and negative z).

- Second, we apply a 90° clockwise-rotation around the x -axis. In this way, $y=0$ becomes the new equatorial plane (and reflection symmetry plane) of the BNS merger simulation, while the y -axis becomes the new orbital axis. This avoids dealing with the singularity at $\theta=0$ in our spherical coordinate system.
- Then, data are imported in PLUTO and interpolated onto a 3D spherical coordinate grid where we remove the region $r < r_{\text{exc}} (= 380 \text{ km})$. A logarithmic increase in the grid spacing along the radial direction is adopted, allowing us to retain high resolution close to the inner boundary, where it is required, while significantly lowering the number of grid points at larger and larger distances.
- The artificial density floor or “atmosphere” employed in the BNS merger simulation ($\approx 6.3 \times 10^4 \text{ g/cm}^3$) is appropriate within a distance of order $\sim 1000 \text{ km}$, but at larger scales it needs to be replaced with a medium with density and pressure that rapidly decrease with distance. More specifically, we import density and pressure values in the region $r_{\text{exc}} \leq r < 1477 \text{ km}$, while at larger radii we replace the artificial floor contribution with a function decaying as r^{-a} , where $a = 5$. At $r > 2500 \text{ km}$, we only retain such decaying artificial atmosphere and do not use anymore data imported from the BNS merger simulation. In this way, we have the freedom to fill the remaining computational domain up to the outer radial boundary, which is set to $r_{\text{max}} = 2.5 \times 10^6 \text{ km}$. In Appendix A, we analyze the impact of the atmosphere on the final outcome of our simulations by showing the results obtained with different power-law exponents for the decaying density and pressure.

As an example of the PostCactus interpolation, we report in the left panel of Fig. 1 the results obtained for the rest-mass density at 101 ms after merger. On the right panel of the same Figure, we show instead the final result of the procedure discussed above to import data into the PLUTO computational grid. To better illustrate the corresponding atmosphere replacement, we also show in Figure 2 the radial profiles of the rest-mass density along the x - and y -axes.

The physical quantities from the BNS merger simulation that are used for setting up the initial data are rest-mass density, pressure,

and 3-velocities, while the specific internal energy is recomputed via the EOS. In PLUTO, we employ the Taub EOS, which corresponds to an ideal gas EOS with $\Gamma = 4/3$ in the highly relativistic limit and $\Gamma = 5/3$ in the non-relativistic limit, with a smooth and continuous behaviour at intermediate regimes (Mignone & McKinney 2007). Since this EOS does not match exactly the EOS of the BNS merger simulation at the low densities of interest, the specific internal energy in the PLUTO setup does not coincide with the one of the original BNS merger data. In order to ensure that such a mismatch has no relevant impact on the final conclusions of our study, we performed twice the same simulation where either (i) the pressure is directly imported and the specific internal energy is derived from the Taub EOS or (ii) the opposite. The comparison is discussed in Appendix B.

As fiducial resolution, we adopt $756 \times 252 \times 504$ points along r , θ , and ϕ , respectively. With a logarithmic radial grid, this yields the smallest grid spacing (at $r_{\text{exc}} = 380 \text{ km}$) of $\Delta r \approx 4.4 \text{ km}$, $r\Delta\theta \approx 4.4 \text{ km}$, and $r\Delta\phi \approx 4.7 \text{ km}$. We also note that, to avoid the polar axis singularity, θ varies within the range $[0.1, \pi - 0.1]$, while ϕ covers the whole $[0, 2\pi]$ interval. A resolution study is presented in Appendix C, where we show results for the same model with four different resolutions (including the fiducial one).

2.2 Gravity, pressure gradients, and boundary conditions

While general relativistic effects are not important at $r \gtrsim 380 \text{ km}$, the (Newtonian) gravitational pull from the central object remains an ingredient that must be taken into account. In particular, gravity causes the fall-back of the inner part of the slowly expanding material that constitutes the surrounding environment through which the incipient jet has to drill and, as we demonstrate in Section 3.2, this has an impact on the final jet energetics and collimation. For this reason, we introduce the Newtonian gravitational acceleration

$$\vec{g} = -G \frac{M_0}{r^2} \hat{r}, \quad (1)$$

where M_0 is the gravitational mass of the merger remnant (specified above) and G is the gravitational constant.

As shown by the post-merger dynamics obtained from the BNS merger simulation, the angular and radial distribution and the slow

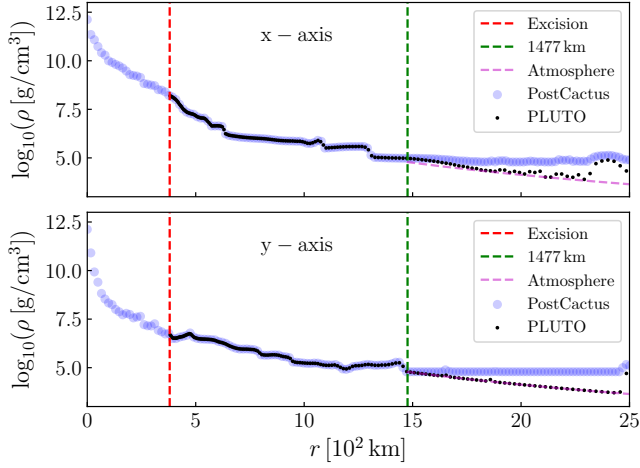


Figure 2. Radial profile of the rest-mass density along the x - and y -axes for data imported from the reference BNS merger simulation at 101 ms post-merger. The blue and black dots refer to the result of the PostCactus interpolation and to the final setup in PLUTO, respectively. The vertical red- and green-dashed lines indicate, respectively, the excision radius and the radial distance (1477 km) above which we replace the uniform artificial density floor with a profile decaying as r^{-5} (shown with a magenta-dashed line). See text for further details.

expansion of the material surrounding the remnant NS are the result of the combined action of gravitational pull, centrifugal support, and pressure gradients. Since in our PLUTO simulations we excise the inner region ($r < r_{\text{exc}} = 380$ km), part of the outward push associated with the radial gradients of pressure is not accounted for. In order to compensate for this, we introduce, along with gravity, an outward directed acceleration⁴. Having the full BNS merger simulation to compare with, we had the opportunity to test different prescriptions, finally adopting the one described in the following. In Appendix D, we show an example test demonstrating that such a prescription captures well the dynamics of the system at $r \geq 380$ km.

The additional outward acceleration term has the form of a gravitational force with opposite sign, i.e.

$$\vec{a} = G \frac{M_{\text{eff}}(r, t)}{r^2} \hat{r}, \quad (2)$$

where the “effective” mass M_{eff} is a function of both the radial coordinate and time. At the excision radius (r_{exc}) and at the time of data import (t_{in}), we set

$$M_{\text{eff}}(r_{\text{exc}}, t_{\text{in}}) = - \left[r^2 \frac{1}{\bar{\rho} G} \frac{d\bar{P}}{dr} \right]_{r_{\text{exc}}, t_{\text{in}}}, \quad (3)$$

where \bar{P} and $\bar{\rho}$ are the angular-averaged pressure and rest-mass density extracted from the BNS merger simulation. The time dependence of the effective mass at r_{exc} is obtained by extracting the corresponding value at different times from the original simulation and then fitting the resulting profile with a simple function (in the example case discussed in Appendix D, for instance, an exponential decay gives a

fairly good fit; see also Figure 10). Once $M_{\text{eff}}(r_{\text{exc}}, t)$ has been obtained, the radial dependence is set as a linear decrease such that the effective mass becomes zero at a characteristic radius $r^* = 700$ km, i.e.

$$M_{\text{eff}}(r, t) = \begin{cases} M_{\text{eff}}(r_{\text{exc}}, t) \frac{r^* - r}{r^* - r_{\text{exc}}} & \text{if } r_{\text{exc}} \leq r \leq r^* \\ 0 & \text{if } r > r^* \end{cases}. \quad (4)$$

We complement the prescription with the following boundary conditions. Exploiting the fact that in the time window of interest (from about 100 to a few hundred ms after merger) the matter outflows are nearly stationary at $r_{\text{exc}} = 380$ km, we assume that pressure, rest-mass density, and velocities are constant in time over the excision surface. We adopt instead zero-gradient (i.e. “outflow”) boundary conditions at the outer radius of the computational domain. For θ and ϕ coordinates, we impose zero-gradient and periodic boundary conditions, respectively.

The above settings apply to an evolution where no collapse to a BH occurs (nor a jet is launched) and, as such, could be directly tested against the evolution given by the original BNS merger simulation (Appendix D). The same settings can also be used to extrapolate the system evolution beyond the time covered by the original simulation (see Section 4). When the remnant NS is assumed to collapse, however, the prescription has to be properly modified to account for the formation of a BH-disk system (inside the excised region), which causes a rapid decrease of the outward push associated with radial pressure gradients. In particular, we introduce the following exponential decay of the effective mass:

$$M_{\text{eff}}(r, t) = M_{\text{eff}}(r, t_c) \exp\left(-\frac{t - t_c}{\tau}\right), \quad (5)$$

where t_c is the collapse time and τ is defined as

$$\tau \equiv \tau_j - (\tau_d - \tau_j) \sin^2 \alpha, \quad (6)$$

with α the angle with respect to the orbital axis (or the remnant/BH spin axis, i.e. $\theta, \phi = \pi/2$). In the above expression, τ_d is the accretion timescale of the BH-disk system, while τ_j is a characteristic timescale connected to the delay between the collapse and the jet launching time. Along the BH spin axis, matter is rapidly accreted on a timescale τ_j , allowing the jet to emerge, while on the orbital plane, matter accretes on the much longer timescale τ_d . In this work, we set $\tau_j = 14.5$ ms and $\tau_d = 0.3$ s, which is consistent in order of magnitude with what found in BNS merger simulations (e.g., Ruiz et al. 2016). After collapse, also the radial boundary condition at the excision radius is set to zero-gradient, allowing matter to fall inside the excised region as a consequence of the gravitational pull.

2.3 Jet injection

In our PLUTO simulations, an incipient relativistic jet is introduced into the system from the inner radial boundary ($r_{\text{exc}} = 380$ km), starting 11 ms after the time chosen for the collapse of the remnant NS. We assume a time-dependent “top-hat” (i.e. uniform) jet contained within a half-opening angle of 10° from the y -axis, which corresponds to the direction orthogonal to the orbital plane of the BNS merger. The injection is two-sided, with identical properties in the $y > 0$ and $y < 0$ regions (we recall that the simulation is in full 3D, without imposed symmetries). Outside the injection angle, radial boundary conditions at r_{exc} are kept as zero-gradient for the rest-mass density, pressure, and angular components of the 3-velocity (v_θ, v_ϕ). The radial velocity obeys to the same condition as long as $v_r < 0$, otherwise we set $v_r = 0$. Moreover, to ensure numerical stability near the injection region, we change the reconstruction to the

⁴ External forces (including gravity and the force resulting from radial pressure gradients) are introduced in our simulations using the `BodyForceVector()` function provided by PLUTO. In order to consistently treat them in the special relativistic case, we corrected the relevant equations in the latest PLUTO release (version 4.4). More details can be found in the PLUTO User’s Guide at <http://plutocode.ph.unito.it/documentation.html>.

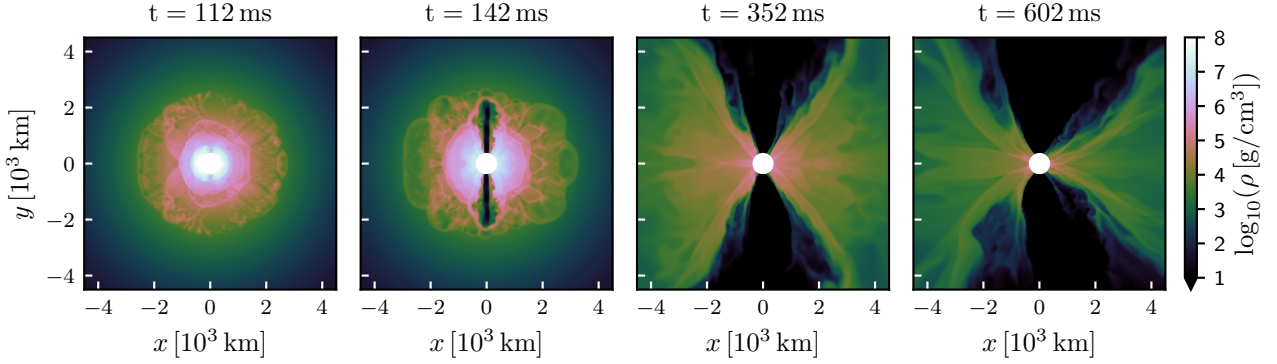


Figure 3. Meridional view of the rest-mass density at different times for our fiducial model (see Section 3.1). Left panel refers to the initial jet launching time. As in Fig. 1, the white circle of 380 km radius corresponds to the excised region.

more dissipative piecewise linear for $r_{\text{exc}} \leq r < 385$ km and within an angular distance of 30° from the y -axis.

For the incipient jet properties at the initial injection time, we set a Lorentz factor $\Gamma_0 = 3$ (with purely radial outgoing motion), a specific enthalpy $h_0 = 100$ (corresponding to a terminal Lorentz factor $\Gamma_\infty \equiv h_0 \Gamma_0 = 300$), and a two-sided luminosity of

$$L_0 = 4\pi r_{\text{exc}}^2 \int_0^{\alpha_j} (h_0 \Gamma_0^2 \rho_0 c^2 - P_0) v_0 \sin \alpha' d\alpha' = 3 \times 10^{50} \text{ erg/s}, \quad (7)$$

where α' is the angle with respect to the jet axis, α_j is the jet half-opening angle in radians, v_0 is the radial velocity (corresponding to $\Gamma_0 = 3$), and ρ_0 and P_0 are the comoving rest-mass density and pressure, respectively. In the above expression, P_0 is determined from ρ_0 and h_0 via the Taub EOS. Therefore, ρ_0 is the only remaining free parameter and can be adjusted to give the desired L_0 .

We then impose an exponential time decay in luminosity $L(t) = L_0 e^{-t/\tau_d}$, with characteristic timescale $\tau_d = 0.3$ s (the same as the BH-disk accretion timescale; see Section 2.2). Such a decay in luminosity is achieved by means of an exponential decay with double characteristic timescale $2\tau_d$ in both the incipient jet radial velocity v_0 and the term $(h_0 \Gamma_0^2 \rho_0 c^2 - P_0)$.

The above incipient jet properties, which are within the expected range for a SGRB jet (e.g., Lazzati et al. 2020 and refs. therein), are employed in all the simulations discussed in this work. Investigating the effects of different injection properties is beyond our present scope and will be the subject of future studies.

3 COLLAPSE AT 0.1 SECONDS AFTER MERGER

In this Section, we discuss the outcome of simulations where we set the collapse time of the remnant NS to 101 ms after merger. The evolution is followed up to slightly more than 1 s after merger. We start by discussing our fiducial model, where the prescriptions presented in Section 2 are applied in full. In addition, we consider two more simulations, one where we do not include the external forces (i.e. the gravitational pull and the outward acceleration accounting for radial pressure gradients; see Section 2.2) and another one where we additionally replace the post-merger environment with a spherically symmetric matter distribution in homologous expansion, as often assumed in SGRB jet propagation models.

3.1 Fiducial model

For our first jet simulation in PLUTO (hereafter “fiducial” case or model), we started from BNS merger data imported at 101 ms post-merger as described in Section 2.1. The corresponding initial data for the rest-mass density are shown in the right panel of Figure 1. The excised region (of radius 380 km) is surrounded by a slowly expanding (maximum radial velocity $\approx 0.07 c$) cloud of material of mass $\approx 0.02 M_\odot$ and with density declining by a few orders of magnitude up a scale of ~ 2 km. The higher density inner region ($380 \text{ km} \leq r \leq 500 \text{ km}$) presents a significant deviation from an isotropic distribution, with a lower density funnel along the orbital axis (or remnant NS spin axis). This is a common feature observed in BNS merger simulations (e.g., Cioffi 2020c and refs. therein), resulting from the combination of the gravitational pull and the non-isotropic centrifugal support and pressure gradients. As we discuss in this Section, the presence of such a funnel can significantly affect the initial propagation of an incipient jet.

Following the prescriptions described in the previous Section 2, we assume that 101 ms is the time at which the remnant NS collapses to a BH. After 11 ms of evolution accounting for the formation of a central BH-disk system, i.e. at 112 ms after merger, we inject into the system a relativistic beam with the chosen properties (specified in Section 2.3). In the first panel of Fig. 3, we show the rest-mass density distribution at the initial time of injection. Due to the further outflow of matter emerging from the excision surface, the total mass of the surrounding environment is about 30% larger with respect to 101 ms. In Fig. 4, we report the angle-averaged rest-mass density, pressure and radial velocity at the same time. From the right panel, we notice that the expansion is nearly homologous up to more than 600 km.

As the incipient jet starts to propagate through the surrounding environment, a high collimation is maintained up to the breakout time, around 30 ms later (Fig. 3, second panel). As the injection continues, more and more energy is transferred laterally to the material surrounding the jet, leading to a hot and high-pressure interface (or cocoon) and eventually to an emerging jet with a certain angular structure (see below). On small scales, the ensuing evolution is characterized by a widening of the low density funnel excavated by the jet (Fig. 3, third and fourth panels), due to a changing pressure balance with the surrounding material. An important contribution to this effect is given by the continuous accretion of the innermost and most dense material. At 200 ms after merger, for instance, the mass outside the excised region has already decreased by a factor of ≈ 4 .

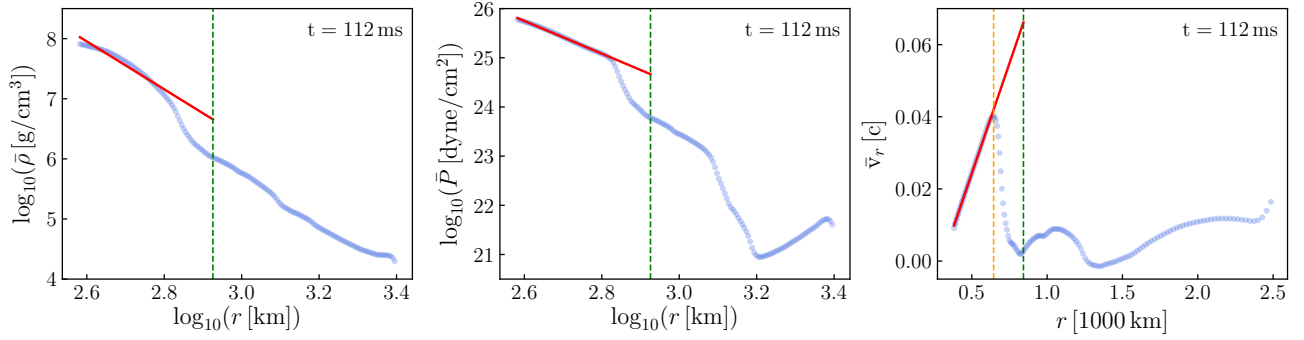


Figure 4. Radial profiles of the angle-averaged rest-mass density, pressure, and radial velocity at 112 ms after merger in our fiducial simulation (blue dots). Red lines represent the analytical fits described in Section 3.3. The vertical orange dashed line in the right panel marks the distance up to which the nearly homologous expansion regime holds. In all panels, the vertical green dashed line marks the distance at which the analytic density profile gives the same total mass of the environment as the original data.

Along with the above widening effect, the evolution on small scales also reveals the development of Kelvin-Helmholtz instability vortices at the jet-cocoon interface, which lead to episodes of increased baryon loading of the funnel due to portions of material that are occasionally brought in (see, e.g., [Gottlieb et al. 2019](#) for a discussion of a similar process). One of this episodes is illustrated in Fig. 5 (top panels), where we show a meridional view of rest-mass density and Lorentz factor at 462 ms after merger. Such a process perturbs the recollimation shock at the base of the jet, contributing to the development of intermittency and deviations from axisymmetry, and reducing both the collimation and the overall efficiency in converting the injected power into radial kinetic energy.

Figure 6 (upper panels) shows in full scale (order $\sim 10^5$ km) the rest-mass density, internal energy density, and Lorentz factor at the end of the simulation, i.e. 1012 ms after merger. At this time, the injection power has significantly declined ($L(t) \propto e^{-t/\tau_d}$ with $\tau_d = 0.3$ s) and the jet is composed by an ultra-relativistic “head” (hereafter referring to the outer high Lorentz factor portion of the outflow) whose front has reached $\approx 2.7 \times 10^5$ km, followed by a less collimated, slower, hotter, and more turbulent tail. The maximum Lorentz factor at the jet’s head is $\Gamma \approx 40$. From the meridional view of the Lorentz factor (Fig. 6, top right panel), we also notice clear deviations from axisymmetry. This reflects the fact that the surrounding environment imported from the BNS merger simulation is not perfectly axisymmetric and the following evolution amplifies further such deviations.

Figure 7 (top panel) shows the radial profile of the Lorentz factor at 1012 ms after merger, where the maximum value is reported for each radius. At the jet’s head, north and south profiles are nearly identical to each other. We also investigate the angular dependence of the Lorentz factor at the jet’s head (and at 1012 ms after merger), by computing the radial-average $\bar{\Gamma}$ within the interval $r \in (24, 27) \times 10^4$ km along different directions. In particular, we consider the cone of constant $\theta \approx 89^\circ$, i.e. the θ value corresponding to the maximum Γ direction, and vary the ϕ coordinate (note that for $\theta = 90^\circ$, this would give the angular profile on the xy -plane).⁵ The profile is given in terms of the angle α , measuring the angular distance from the injection axis (or y -axis) and with positive/negative sign for positive/negative x . The result for the north side is shown in the top panel of Fig. 8 (south

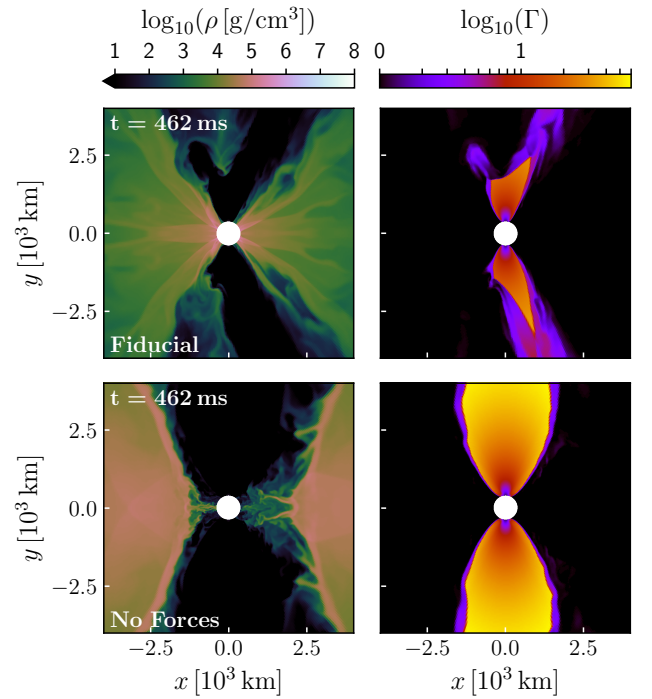


Figure 5. Meridional view of rest-mass density (left) and Lorentz factor (right) at 462 ms after merger. Top and bottom rows refer to the fiducial simulation (Sect. 3.1) and to the one without external forces (Sect. 3.2), respectively.

profile is essentially coincident). A deviation of $\approx 0.9^\circ$ from the injection axis is observed for the direction containing the maximum Lorentz factor. Moreover, we find that the angular profile cannot be reproduced by a simple Gaussian or power-law function. In particular, the central peak ($\bar{\Gamma} \gtrsim 27$) can be nicely fit with a skewed function

$$S(\alpha) \propto e^{-\frac{(\alpha-\bar{\alpha})^2}{2\sigma^2}} \left[1 + \operatorname{erf} \left(\beta \frac{(\alpha-\bar{\alpha})^2}{2\sigma^2} \right) \right], \quad (8)$$

with $\sigma = 3.6^\circ$ (analogous to the Gaussian σ parameter), the skewness parameter $\beta = 3.55$, and $\bar{\alpha} = -0.69^\circ$. However, the overall profile

⁵ We recall that the spherical coordinates are tilted with respect to the jet injection axis, with the latter corresponding to $\theta = 90^\circ$ and $\phi = 90^\circ$ (on the north side).

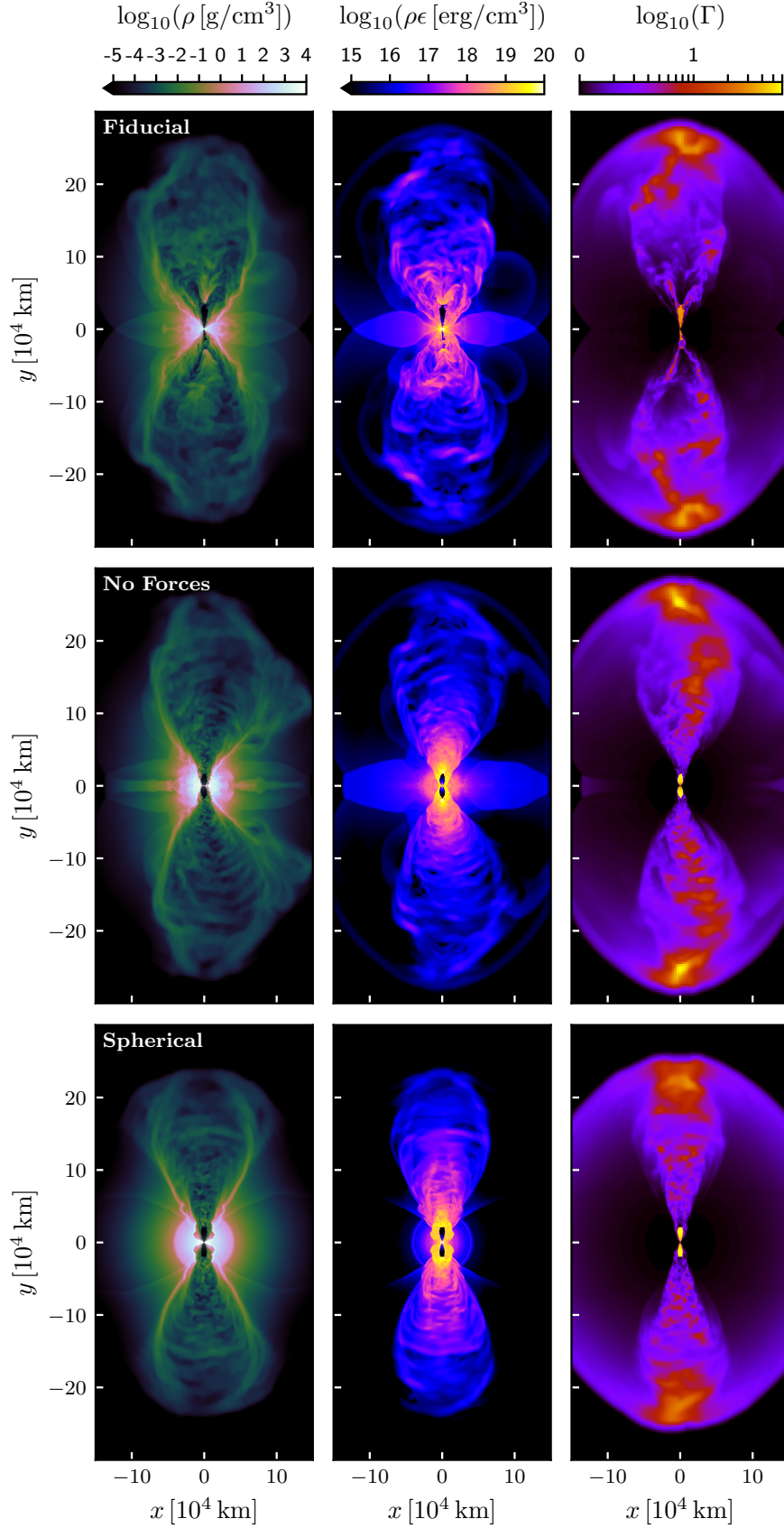


Figure 6. Meridional view of rest-mass density, internal energy density, and Lorentz factor at 1012 ms after merger (left to right). Top, central, and bottom rows refer to the fiducial simulation (Sect. 3.1), the one without external forces (Sect. 3.2), and the one with simplified isotropic environment (Sect. 3.3), respectively.

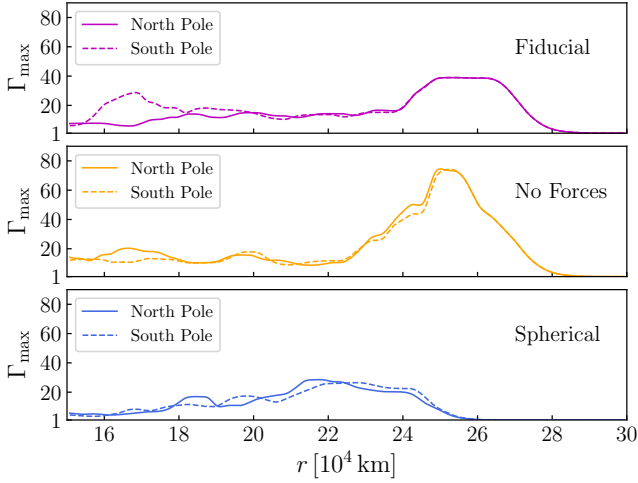


Figure 7. Radial profiles of maximum Lorentz factor at 1012 ms after merger (maximum value achieved at each radial distance). North and south profiles are shown for the same three cases of Fig. 6: our fiducial simulation (top), the one without external forces (center), and the one with simplified isotropic surrounding environment (bottom).

presents highly asymmetric lateral wings that cannot be neglected when considering the jet energetics (see below).

We also analyze the energy content of the emerging outflow (in the region $r > 3000$ km) at 1012 ms after merger. The total kinetic energy is $\approx 3.7 \times 10^{49}$ erg, while the internal energy is $\approx 5.4 \times 10^{48}$ erg, i.e. about 15% of the kinetic one. This ratio confirms a substantial (but not yet complete) conversion of heat into outflowing motion. The sum of the above kinetic and internal energies accounts for $\approx 48.5\%$ of the total injected energy ($\approx 8.7 \times 10^{49}$ erg), where about half of the latter is instead lost due to the gravitational pull acting on the environment material (see also the next Section, where the effects of removing the gravitational pull are discussed).

At the jet’s head, taking as a reference the shell given by the radial interval $r \in (24, 27) \times 10^4$ km and defining the “core” as the region within an angle of $\sigma = 3.6^\circ$ from the maximum Lorentz factor direction, we obtain

$$\begin{aligned} E_{\text{kin,core}} &\approx 2.947 \times 10^{48} \text{ erg}, & E_{\text{kin,shell}} &\approx 6.806 \times 10^{48} \text{ erg}, \\ E_{\text{tot,core}} &\approx 3.790 \times 10^{48} \text{ erg}, & E_{\text{tot,shell}} &\approx 8.842 \times 10^{48} \text{ erg}. \end{aligned}$$

In the core, kinetic energy contributes to 78% of the total energy. The contribution of the core total energy compared to the whole shell is $\approx 43\%$.

The bottom panel of Fig. 8 shows the angular profile of the isotropic equivalent energy E_{iso} (kinetic plus internal) of the jet’s head, i.e. within the radial interval $r \in (24, 27) \times 10^4$ km. Also in this case, only the profile on the north side is reported, since the one on the south side is nearly coincident. As for the radial-averaged Lorentz factor, the E_{iso} angular profile is characterized by a slightly offset and asymmetric central peak that is well reproduced by a skewed function and by additional lateral wings that are highly asymmetric. In particular, the peak ($E_{\text{iso}} \approx 2.8 \times 10^{51}$ erg) occurs about 0.8° away from the injection axis and the best-fitting width parameter is $\sigma \approx 2.1^\circ$.

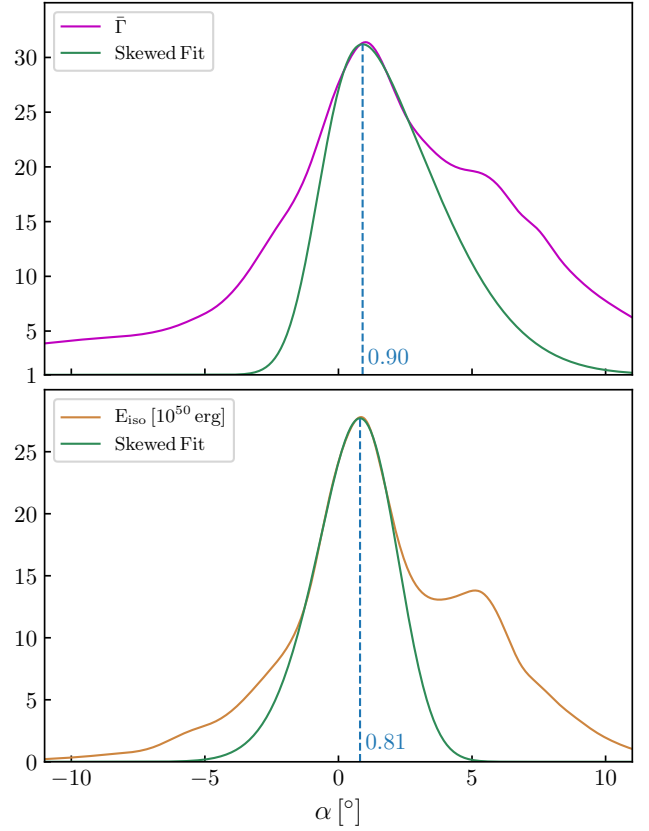


Figure 8. Angular profiles (north side only) of the radial-averaged Lorentz factor (top) and isotropic-equivalent energy E_{iso} (bottom) at the jet’s head (see text for details), for our fiducial simulation at 1012 ms after merger. Here, α is the angle with respect to the injection axis, obtained by varying the ϕ coordinate at fixed $\theta \approx 89^\circ$. The green curve in both panels correspond to the skewed function that best-fits the central peak of the profile. The vertical dashed blue line marks the angular position of the peak, i.e. 0.90° and 0.81° for the top and bottom panels, respectively.

3.2 Impact of external forces

Our second simulation is analogous to the fiducial one (discussed in the previous Section), except that in this case we switch off the acceleration terms that account for the gravitational pull and the radial pressure gradients (see Section 2.2). Although the inclusion of the above external forces makes the simulations arguably more consistent, the corresponding effects are commonly neglected in SGRB jet propagation studies (excluding those based on general relativistic simulations, e.g. Kathirgamaraju et al. 2019; Nathanail et al. 2021). Here, we aim at assessing whether this choice might have a significant impact on the final jet properties.

A visual comparison at the final simulation time (1012 ms after merger) is provided in Fig. 6, where the upper row refers to the fiducial model, while the central row refers to the simulation without external forces. Looking at the rest-mass density close to the excision surface, we note that in the latter case a more massive environment surrounds the low density funnel, due to the fact that in absence of a gravitational pull material does not fall back towards the center nor gets accreted. As a consequence, not only the widening effect depicted in Fig. 3 is substantially reduced, maintaining a higher degree of collimation, but also the generation of Kelvin-Helmholtz

instabilities discussed in the previous Section is strongly inhibited. To illustrate this, in the bottom panels of Fig. 5 we show the rest-mass density and Lorentz factor on the meridional plane at 462 ms after merger, to be compared with the fiducial case in the top panels of the same Figure. The shear at the jet-cocoon interface is much more stable and no episodic baryon loading of the funnel is noticed. This results in an essentially unperturbed recollimation shock, which allows the incipient jet to preserve a higher and more stable Lorentz factor. At the same time, the internal energy density (see Fig. 6) reveals a hotter and more uniform outflow up to $\sim 10^5$ km.

At the end of the simulation (see Fig. 6), the jet reaches a maximum Lorentz factor almost a factor of 2 higher than the fiducial case, as also reported in Fig. 7. The acceleration, on the other hand, is more gradual and the distance reached by the outflow at the final time is similar (if not even slightly smaller). Moreover, because of the higher and more persistent collimation and Lorentz factor at the base of the outflow, the jet's head is now followed by a rather well-defined tail extending down to the excision surface.

Computing the internal and kinetic energies of the emerging outflow for $r > 3000$ km and at 1012 ms after merger, we find that they sum up to $\approx 1.1 \times 10^{50}$ erg, i.e. about 127% of the total injected energy. On the one hand, this indicates that the absence of the gravitational pull, unlike the fiducial case, preserves the injected energy. On the other hand, it shows that additional energy residing in the initial environment is carried along by the incipient jet.

From this example, we conclude that neglecting the external forces (including gravity) can have major effects on the final outcome.

3.3 Realistic versus simplified environment

For the simulation discussed in this Section, we further reduce the degree of realism by not only neglecting the external forces (like in the previous Section), but also substituting the matter distribution and velocities of the surrounding environment imported from the BNS merger simulation with simpler analytic prescriptions. In particular, we adopt the common assumptions of (i) a spherically symmetric matter distribution with density and pressure decreasing with radius as a power-law and (ii) homologous expansion.

In order to produce an initial setup with the above assumptions that is the closest to what we have in the case of imported BNS merger data, we fit the angle-averaged rest-mass density and pressure at 112 ms after merger with power-law radial functions. Similarly, we fit the angle-averaged radial velocity with a linear function of the radius. We limit the fits within a distance of ≈ 645 km, up to which the three angle-averaged profiles are rather well reproduced (Fig. 4). The resulting analytical functions are:

$$\bar{\rho}_{\text{fit}}(r) = 1.056 \times 10^8 \times \left(\frac{r}{380 \text{ km}}\right)^{-3.981} \text{ g/cm}^3 \quad (9)$$

$$\bar{P}_{\text{fit}}(r) = 6.408 \times 10^{25} \times \left(\frac{r}{380 \text{ km}}\right)^{-3.320} \text{ dyne/cm}^2 \quad (10)$$

$$\bar{v}_{\text{fit}}(r)/c = 0.047 \times \left(\frac{r}{380 \text{ km}}\right) - 0.037. \quad (11)$$

Then, for our simulation setup, we impose an isotropic environment following the above profiles and extended up to a radial distance of ≈ 843 km. Such a distance is chosen in order to have a total mass of the environment equal to the one in the fiducial simulation. Finally, we add an artificial atmosphere identical to the one imposed in the fiducial case (see Section 2.1).

Figures 6 and 7 (bottom row) show the simulation results in terms of rest-mass density, internal energy density, and Lorentz factor at the final time of 1012 ms after merger. To evaluate the effects of a

simplified analytical and isotropic environment, we compare with the results of the previous simulation (without external forces, central row in Figs. 6 and 7). The impact is substantial. The absence of a lower density funnel along the injection axis in the surrounding material makes it much harder for the jet to emerge, resulting in a breakout time delayed by ≈ 100 ms, a final maximum Lorentz factor around 30 (more than a factor of 2 lower and notably with a non-negligible north/south difference), and a jet's head that has reached only $\approx 2.5 \times 10^5$ km at its front. The jet remains rather collimated and the emerging structure is well aligned with the injection axis and nearly axisymmetric.

These results indicate that simplified analytical prescriptions for the surrounding environment, corresponding to what is often assumed, may substantially weigh on the jet dynamics and morphology when compared to the more realistic conditions obtained in BNS merger simulations.

4 COLLAPSE AT 0.2 SECONDS AFTER MERGER

In this Section, we discuss the results of a simulation with collapse time of the remnant NS set to 201 ms after merger. Unlike the fiducial case presented in Section 3.1, here the collapse time is not covered by the BNS merger simulation, which is limited to 156 ms. Therefore, in order to obtain the initial data for the following incipient jet evolution, we first need to continue or extrapolate the evolution from 156 to 201 ms. We treat such a case with a double purpose: (i) showing the feasibility of this kind of extrapolation and (ii) investigating the effect of a significantly different remnant NS lifetime (by a factor 2 in this case).

The data imported at the latest available time of the BNS merger simulation provide a different environment around the remnant NS. Fig. 9 (left panel) shows in particular the rest-mass density at that time. Compared to 101 ms post-merger (Fig. 3), we observe a larger cloud of slowly expanding material resulting from the nearly isotropic baryon-loaded wind from the remnant NS. Radial motion is nearly homologous and radial velocity reaches a maximum of $\approx 0.03 c$ at $\approx 1.5 \times 10^3$ km. The inner and higher density region up to ≈ 500 km remains rather unchanged and a lower density funnel along the y-axis is still present.

In order to evolve the system in PLUTO from 156 to 201 ms post-merger, we follow the prescriptions given in Section 2.2 (with no collapse, nor jet injection), where the extra acceleration due to radial pressure gradients needs to be specified in terms of the effective mass M_{eff} and its time evolution (see Eq. 3 and Section 2.2). As shown in Fig. 10, the BNS merger simulation reveals a clear decreasing trend in the radial pressure gradients, which corresponds to a decreasing effective mass at the excision radius. An exponential decay with characteristic damping time of 58.8 ms reproduces well the decreasing profile. Adopting the corresponding fitting function for later times (≥ 156 ms), we have the necessary input to continue the evolution up to 201 ms.

For verification purposes, we checked our prescription for the effective mass (including the exponential fitting function) by importing data into the PLUTO code at the earlier time 141 ms after merger and then evolving up to 156 ms for a direct comparison with the original BNS merger simulation. The comparison, discussed in Appendix D, shows a very good agreement and gives us confidence to proceed with the evolution from 156 to 201 ms.

At 201 ms post-merger, the remnant NS is assumed to collapse and the following evolution consists, as in the fiducial case and the other cases discussed in Section 3, of 11 ms of post-collapse rearrangement

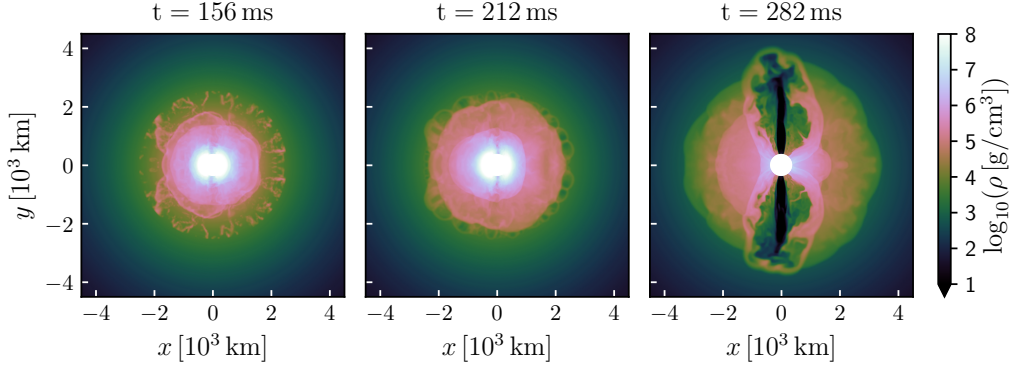


Figure 9. Same as Fig. 3 for the model with collapse at 201 ms (and jet launching at 212 ms).

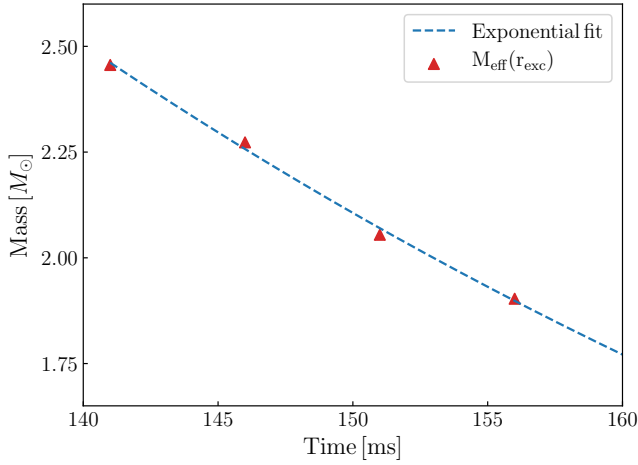


Figure 10. Evolution of the effective mass at the excision radius (380 km) at times ≥ 141 ms after merger. Red triangles are the values of $M_{\text{eff}}(r_{\text{exc}})$ extracted from the BNS merger simulation, while the dashed blue curve corresponds to an exponential fit (see text).

and the subsequent jet injection. Also in this case, the simulation covers up to 900 ms after the jet launching time, i.e. up to 1112 ms after merger. Figure 9 shows the rest-mass density at the time of jet launching and around the time the jet itself breaks out of the surrounding environment (central and right panels, respectively). We note that the total rest mass outside the excised region at the jet launching time ($\approx 4.1 \times 10^{-2} M_{\odot}$) is a factor ≈ 2 larger than in our fiducial model, consistently with the doubling of the remnant NS lifetime. As a consequence, the incipient jet takes more than twice the time to break out (≈ 70 ms instead of ≈ 30 ms).

The effects of a longer NS lifetime and a later jet launching on the final jet structure (900 ms after jet launching) can be appreciated in Figure 11, where we show the rest-mass density and the Lorentz factor at large scales on the xy -plane. Even though the jet injection parameters are the same as in the fiducial model, we observe important differences that are to be attributed to the different initial environment. The jet needs to drill through a more massive and extended cloud of material, spending more power to break out and reaching, after 900 ms, a significantly smaller radial distance (jet’s head front is located at $\approx 2.5 \times 10^5$ km, to be compared with $\approx 2.7 \times 10^5$ km of the fiducial model). Also the maximum Lorentz factor at the jet’s

head is smaller (≈ 35 instead of ≈ 40). At the same time, the denser environment close to the excision surface maintains a higher degree of collimation and axisymmetry in the outflow, also resulting in a more compact jet’s head.

For a given BNS merger model, the time interval between merger and jet launching is confirmed as a key parameter in determining the ultimate jet structure, which, in turn, shapes the corresponding radiative signatures. This offers good prospects for constraining such a time interval via the comparison with the observations.

5 SUMMARY AND CONCLUSIONS

In this paper, we presented 3D special relativistic hydrodynamic simulations of incipient SGRB jets propagating through the baryon-polluted environment surrounding the remnant of a BNS merger. For the first time, we employ initial data for the environment obtained by directly importing the outcome (i.e. density, pressure, and velocity distributions) of a general relativistic BNS merger simulation. This represents a first key step towards a consistent end-to-end description connecting the details of a specific BNS merger with the ultimate EM signatures associated with the breakout and propagation of an emerging SGRB jet.

The simulations are performed with the PLUTO code, using rotated spherical coordinates (with polar axis lying on the BNS orbital plane) and logarithmic spacing along the radial direction. A central sphere of 380 km radius is excised and suitable boundary conditions are adopted on the corresponding spherical surface. We also include the effects of two external forces: the gravitational pull of the central object (with a mass of $\approx 2.596 M_{\odot}$) and an extra (time and space dependent) radial acceleration term added to compensate for the missing contribution of radial pressure gradients due to the excised region. Inner boundary conditions and prescriptions for the external forces are validated by test simulations comparing the obtained evolution with the original BNS merger simulation results. The computational domain is initially filled with an artificial atmosphere with density and pressure scaling with distance as $\propto r^{-5}$ and zero velocity (also tested along with different choices of the power-law exponent). Finally, we adopt the Taub EOS. Being slightly different from the EOS used in the reference BNS merger simulation (at the low rest-mass densities of interest, i.e. $< 10^8$ g/cm³), small differences arise in the specific internal energy of the initial setup. However, dedicated benchmarks show that the influence on the final outcome is minor.

For the jet injection, we adopt the paradigm in which the central engine powering the relativistic outflow is an accreting BH-disk

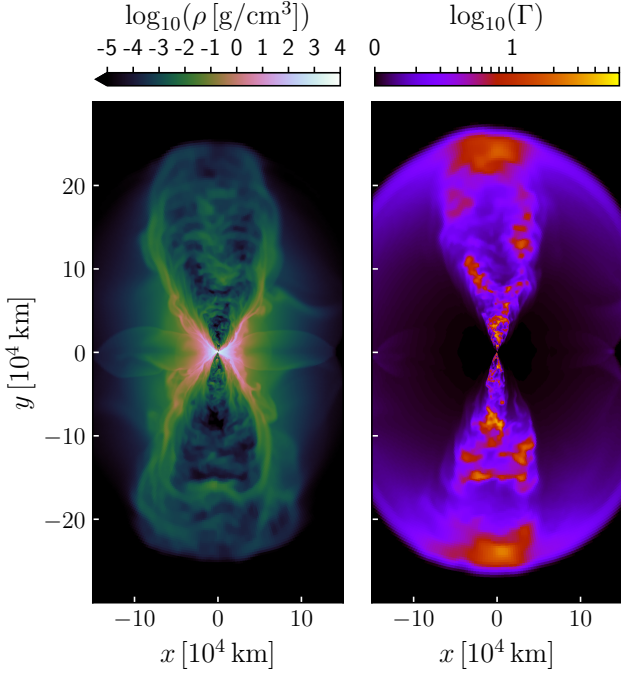


Figure 11. Meridional view of rest-mass density (left) and Lorentz factor (right) at 1112 ms after merger for the case with remnant NS collapse at 201 ms. The spatial and color scales used here are the same adopted in Fig. 6.

system, formed after the eventual collapse of a massive NS remnant. In this work, we assume that the collapse occurs at a chosen time after merger. This is the time at which we import data from the reference BNS merger simulation and start the evolution in PLUTO. To account for the effects of a newly formed BH, we impose a rapid non-isotropic decrease of the extra acceleration added to compensate for the missing radial pressure gradients (see above). This leads the inner part of the environment material, especially along the remnant spin axis, to decelerate its expansion until its motion is reversed and it starts falling back towards the central object. After a time window of 11 ms from the collapse of the remnant NS, the jet is launched.

The incipient jet properties are the same in all our jet simulations. A top-hat outflow is continuously injected from the excision surface and within a half-opening angle of 10° around the remnant spin axis (or orbital axis of the BNS). The initial luminosity, Lorentz factor, and specific enthalpy are $L_0 = 3 \times 10^{50}$ erg/s, $\Gamma_0 = 3$, and $h_0 = 100$, respectively. An exponential time decay in luminosity is enforced with a characteristic timescale of 0.3 s, which is consistent with the order of magnitude of typical accretion timescales of BH-disk systems formed in BNS mergers.

Our simulations probe two different collapse times, namely 101 and 201 ms after merger. For our fiducial case (collapse at 101 ms), we also repeat the simulation without the contribution of external forces (i.e. gravity and extra acceleration compensating for the missing radial pressure gradients) and in one case we also substitute the environment with an isotropic and homologously expanding one.

The main results of our study can be summarized as follows:

- *Realistic post-merger environment.* The density and velocity distributions of the material surrounding the merger remnant at the jet launching time, which depend on the details of the specific BNS system, can deviate significantly from the simplified isotropic and ho-

mologously expanding medium often considered in SGRB jet propagation studies. Comparing a reference model (with 112 ms post-merger jet launching time and no external forces) with an equivalent one where the environment is substituted by the best-fitting isotropic and homologously expanding medium having the same total mass (see Section 3), we find major differences in the outcome. The presence of a lower density funnel along the remnant spin axis allows the incipient jet to breakout more efficiently, retaining a higher energy. This, in turn, results in a much larger maximum Lorentz factor at the jet's head ($\Gamma \gtrsim 70$ vs. ≈ 30 , at 1012 ms after merger) and a lower degree of collimation (in particular in the jet's tail). Another relevant effect is caused by deviations from axisymmetry in the environment (e.g., due to the remnant recoil in unequal mass mergers), which make the final jet slightly misaligned with respect to the orbital axis and non-axisymmetric in structure.⁶

This example poses a strong caveat for any model neglecting the anisotropy in matter distribution of the post-merger environment. Moreover, it shows that the final jet properties can be affected by other features that are typically not considered, such as deviations from axisymmetry or velocity distributions that are more complex than a simple homologous expansion.

- *Impact of external forces.* From the direct comparison with the BNS merger simulation results, we find that a proper description of the environment dynamics should (i) take into account the gravitational pull of the central object and (ii) adequately compensate for the missing contribution of radial pressure gradients due to the presence of an excised inner region. When such external forces are included, the dynamics of the jet propagation is significantly affected. In particular, the surrounding material is allowed to fall back towards the central engine. The falling material directly encountered by the incipient jet acts as an obstacle, dissipating part of the jet energy into heat and turbulent motions. At the same time, accretion keeps reducing the overall mass of the environment, changing the lateral pressure balance between the jet and the surrounding material in favour of the former and leading to a significant widening of the jet's opening angle shortly above the injection radius. The decreasing collimation ultimately results in a more compact jet's head followed by a much wider and slower outflow. Finally, due to the gravitational pull acting on the environment material, the internal and kinetic energies of the emerging outflow only carry about half of the total injected energy. Compared to the equivalent case with no external forces, the maximum Lorentz factor achieved is much lower (almost a factor of 2 at 1012 ms after merger), more energy is deposited in the cocoon, and there is no well defined jet's tail.

In conclusion, the gradual and continuous accretion of the surrounding material, while being overlooked in most SGRB jet propagation models, can have a strong influence on the emerging jet properties.

- *Fiducial model.* Our fiducial simulation, where the remnant NS collapses at 101 ms after merger and the incipient jet is launched 11 ms later, results in a final jet that has successfully emerged from the BNS merger environment. At 1012 ms after merger, the internal-to-kinetic energy ratio of the outflow (for $r > 3000$ km) is about 15%, indicating an advanced stage of conversion of heat into motion. The angular profiles of Lorentz factor and isotropic-equivalent energy at the jet's head reveal a central narrow core (of half-opening angle $\approx 3.6^\circ$ and $\approx 2.1^\circ$, respectively) surrounded by a wider and moderately relativistic outflow carrying a significant fraction of the total energy. The profiles also show the influence of the small deviations from axisym-

⁶ This may also translate in uncertainties in GW-based Hubble constant estimates (e.g., Abbott et al. 2017b; Hotokezaka et al. 2019).

metry in the initial environment: they peak along a direction that is slightly tilted with respect to the injection axis (by $\approx 0.8^\circ - 0.9^\circ$) and the central core and surrounding outflow are slightly and highly non-axisymmetric, respectively. The overall angular dependence cannot be reproduced via simple Gaussian or power-law functions, while a skewed normal function can fit well the central core. This result suggests that employing simple functions to fit SGRB jet angular structures (as revealed, e.g., by afterglow observations) may require some caution.

- *Dependence on the jet launching time.* When considering a jet launching time of 212 ms post-merger (almost double with respect to the fiducial case), the very same incipient jet has to drill through a nearly twice more massive environment. As a consequence, more energy is dissipated into the surrounding material, it takes longer to break out (≈ 70 ms vs. ≈ 30 ms), and the maximum Lorentz factor reached is lower (≈ 35 vs. ≈ 40 at 900 ms after jet launching). On the other hand, the more expanded and massive environment provides a more efficient collimation at the base of the jet, also resulting in a more axisymmetric final structure.

The comparison with the fiducial case confirms that the time interval between merger and jet launching can have a strong influence, which, in turn, implies that tightly constraining such a key parameter via observations is (in principle) possible.

The main aim of this work is to introduce a new approach to address the problem of SGRB jet propagation in BNS merger environments, showing the potential advantages of employing the outcome of BNS merger simulations as initial data. The prescriptions and assumption adopted here, while attempting to offer a more realistic description of some aspects of the system dynamics, leave plenty of room for further improvement. In particular, we do not include magnetic fields, which are a key ingredient in SGRB jet production and evolution. Furthermore, the incipient jet is introduced by hand and not produced self-consistently in the BNS merger simulation. Overcoming the above limitations (among others) should represent a priority in future studies.

ACKNOWLEDGEMENTS

We thank Om Sharan Salafia and Stefano Ascenzi for useful discussions. J.V.K. kindly acknowledges the CARIPARO Foundation for funding his PhD fellowship within the PhD School in Physics at the University of Padova. All the simulations were performed on GALILEO and MARCONI machines at CINECA. In particular, we acknowledge CINECA for the availability of high performance computing resources and support through awards under the ISCRA and the MoU INAF-CINECA initiatives (Grants IsB18_BlueKN, IsB21_SPRITZ, INA20_C6A49, INA20_C7A58) and through a CINECA-INFN agreement, providing the allocations INF20_teongrav and INF21_teongrav.

DATA AVAILABILITY

The data underlying this article will be shared on reasonable request to the corresponding authors.

REFERENCES

- Abbott B. P., et al., 2017a, *Phys. Rev. Lett.*, **119**, 161101
Abbott B. P., et al., 2017b, *Nature*, **551**, 85

- Abbott B. P., et al., 2017c, *Astrophys. J. Lett.*, **848**, L12
Abbott B. P., et al., 2017d, *Astrophys. J. Lett.*, **848**, L13
Abbott B. P., et al., 2019, *Phys. Rev. X*, **9**, 011001
Akmal A., Pandharipande V. R., Ravenhall D. G., 1998, *Phys. Rev. C*, **58**, 1804
Ciolfi R., 2020a, *Mon. Not. R. Astron. Soc. Lett.*,
Ciolfi R., 2020b, *Front. Astron. Sp. Sci.*, **7**, 27
Ciolfi R., 2020c, *Gen. Rel. Grav.*, **52**, 59
Ciolfi R., Kastaun W., Giacomazzo B., Endrizzi A., Siegel D. M., Perna R., 2017, *Phys. Rev. D*, **95**, 063016
Ciolfi R., Kastaun W., Kalinani J. V., Giacomazzo B., 2019, *Phys. Rev. D*, **100**, 023005
Endrizzi A., Ciolfi R., Giacomazzo B., Kastaun W., Kawamura T., 2016, *Class. Quantum Grav.*, **33**, 164001
Geng J.-J., Zhang B., Kölligan A., Kuiper R., Huang Y.-F., 2019, *Astrophys. J. Lett.*, **877**, L40
Ghirlanda G., et al., 2019, *Science*, **363**, 968
Goldstein A., et al., 2017, *Astrophys. J. Lett.*, **848**, L14
Gottlieb O., Levinson A., Nakar E., 2019, *Mon. Not. R. Astron.*, **488**, 1416
Gottlieb O., Nakar E., Bromberg O., 2021, *Mon. Not. R. Astron.*, **500**, 3511
Hallinan G., et al., 2017, *Science*, **358**, 1579
Hamidani H., Ioka K., 2021, *Mon. Not. R. Astron. Soc.*, **500**, 627
Hotokezaka K., Nakar E., Gottlieb O., Nissanke S., Masuda K., Hallinan G., Mooley K. P., Deller A. T., 2019, *Nature Astron.*, **3**, 940
Ioka K., Nakamura T., 2019, *Mon. Not. R. Astron. Soc.*, **487**, 4884
Kathirgamaraju A., Tchekhovskoy A., Giannios D., Barniol Duran R., 2019, *Mon. Not. R. Astron. Soc.*, **484**, L98
Lazzati D., Perna R., Morsony B. J., Lopez-Camara D., Cantiello M., Ciolfi R., Giacomazzo B., Workman J. C., 2018, *Phys. Rev. Lett.*, **120**, 241103
Lazzati D., Ciolfi R., Perna R., 2020, *Astrophys. J.*, **898**, 59
Lyman J. D., et al., 2018, *Nature Astr.*, **2**, 751
Mignone A., McKinney J. C., 2007, *Mon. Not. R. Astron. Soc.*, **378**, 1118
Mignone A., Bodo G., Massaglia S., Matsakos T., Tesileanu O., Zanni C., Ferrari A., 2007, *Astrophys. J. Sup. Series*, **170**, 228
Mignone A., Zanni C., Tzeferacos P., van Straalen B., Colella P., Bodo G., 2012, *Astrophys. J. Sup. Series*, **198**, 7
Mooley K. P., et al., 2018a, *Nature*, **554**, 207
Mooley K. P., et al., 2018b, *Nature*, **561**, 355
Murguía-Berthier A., Ramirez-Ruiz E., De Colle F., Janiuk A., Rosswog S., Lee W. H., 2021, *Astrophys. J.*, **908**, 152
Nakar E., 2020, *Phys. Rep.*, **886**, 1
Nathanail A., Gill R., Porth O., Fromm C. M., Rezzolla L., 2020, *Mon. Not. R. Astron. Soc.*, **495**, 3780
Nathanail A., Gill R., Porth O., Fromm C. M., Rezzolla L., 2021, *Mon. Not. R. Astron. Soc.*, **502**, 1843
Nativi L., Bulla M., Rosswog S., Lundman C., Kowal G., Gizzi D., Lamb G. P., Perego A., 2021, *Mon. Not. R. Astron. Soc.*, **500**, 1772
Perego A., Rosswog S., Cabezón R. M., Korobkin O., Käppeli R., Arcones A., Liebendörfer M., 2014, *Mon. Not. R. Astron. Soc.*, **443**, 3134
Ruiz M., Lang R. N., Paschalidis V., Shapiro S. L., 2016, *Astrophys. J. Lett.*, **824**, L6
Salafia O. S., Barbieri C., Ascenzi S., Toffano M., 2020, *Astron. Astrophys.*, **636**, A105
Savchenko V., et al., 2017, *Astrophys. J. Lett.*, **848**, L15
Troja E., et al., 2017, *Nature*, **551**, 71
Urrutia G., De Colle F., Murguía-Berthier A., Ramirez-Ruiz E., 2021, *Mon. Not. R. Astron. Soc.*,
Xie X., Zrake J., MacFadyen A., 2018, *Astrophys. J.*, **863**, 58

APPENDIX A: DEPENDENCE ON ATMOSPHERE PRESCRIPTION

When setting up the initial conditions for our simulations, we add an artificial atmosphere characterized by radial profiles of density and pressure decaying as r^{-a} (see Sect. 2.1). Here, we investigate the potential impact of such an atmosphere on the jet propagation by

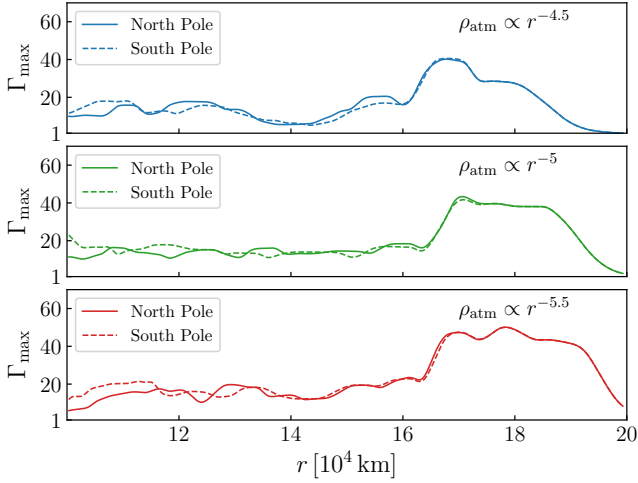


Figure A1. Same as Fig. 6 for our fiducial model with different power-law exponents for the radial profile of density and pressure in the atmosphere, at 762 ms after merger.

considering our fiducial model (Sect. 3.1) with three different values of the power-law exponent a , namely $a=4.5$, 5, and 5.5. In this case, we run the simulations up to 762 ms after merger.

Since the initial atmosphere can represent an obstacle for the emerging jet, the corresponding braking effect is mostly visible when looking at the distance reached by the jet’s head at the latest available time. Figure A1 shows the radial profile of the maximum Lorentz factor (i.e. the maximum reached at given radial distance) at 762 ms after merger. Going from $a = 4.5$ to 5, we notice differences in the jet’s head profile and distance reached. From 5 to 5.5 differences are significantly reduced. We conclude that the power-law exponent should be set to a value of at least 5 (as in our fiducial case).

In order to present quantitatively accurate results, future studies should explore even larger power-law exponents and include any residual atmospheric effects in the error budget.

APPENDIX B: IMPACT OF EOS CHANGE

As pointed out in Section 2.1, the Taub EOS employed in our simulations does not exactly match the EOS used in the BNS merger simulation (at the low densities of interest). This leads to a slight discrepancy in the initial internal energy density, which is recomputed via the Taub EOS from the imported rest-mass density and pressure data values. In order to obtain an indicative measure of the effects on our results, we compare here two simulations: the first one corresponds to our fiducial model (Sect. 3.1), while the second one has an initial setup with imported rest-mass density and specific internal energy (and the pressure is recomputed via the Taub EOS). The latter simulation covers up to 762 ms after merger.

At the level of initial data, the two cases differ by $\approx 7\%$ in (total) internal energy and by $\approx 6\%$ in the sum of kinetic and internal energy. As the system evolves, a significant portion of material falls-back across the excision surface (due to the gravitational pull; Sect. 2.2) and, at the same time, the incipient jet brings in a significant amount of additional internal and kinetic energy. The combination of the two effects makes the initial discrepancy in energy less and less important as the evolution proceeds. Indeed, at 762 ms post-merger, the sum of kinetic and internal energy only differs by $\approx 2\%$ and such a

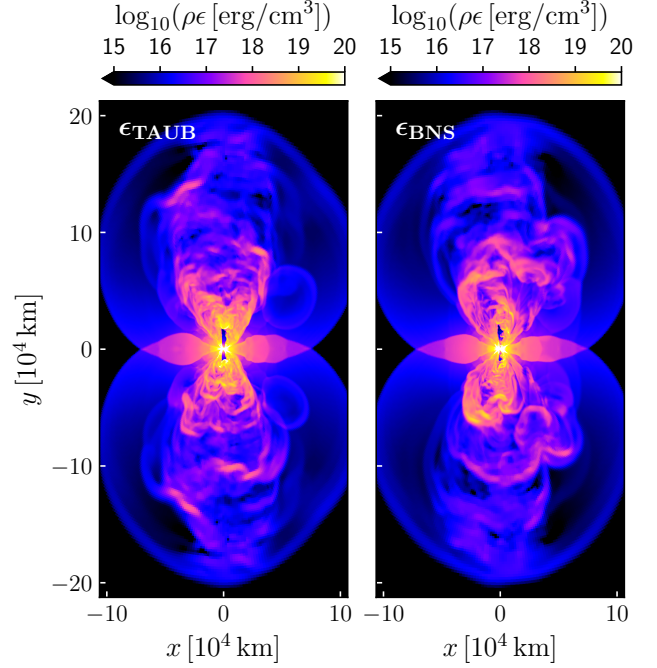


Figure B1. Meridional view of internal energy density at 762 ms after merger. Left panel refers to our fiducial model, where the initial rest-mass density and pressure are directly imported from the reference BNS merger simulation, while the specific internal energy ϵ is derived via the Taub EOS. For the case on the right, the imported quantities are instead rest-mass density and ϵ , while the quantity derived via the Taub EOS is the pressure.

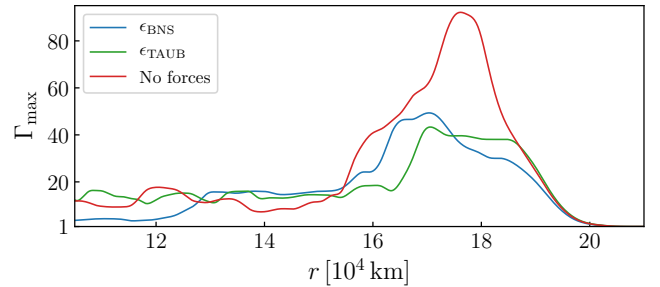


Figure B2. Radial profiles (north side only) of maximum Lorentz factor at 762 ms after merger. The three profiles refer to our fiducial model (ϵ_{Taub}), the one where specific internal energy is directly imported (ϵ_{BNS} ; see text), and the one where no external forces are included.

difference keeps decreasing. Figure B1 shows the comparison for the internal energy density at 762 ms, where no significant differences are present.

As expected from the above considerations, the variation in terms of emerging jet properties is rather limited. In Fig. B2, we report the radial profile of the Lorentz factor (maximum value at each radial distance) at 762 ms. The radial location and profile of the jet’s head is found to be rather similar and the difference in the overall maximum is $\sim 10\%$. For comparison, we also show the case where no external forces are considered (with specific internal energy recomputed via the Taub EOS; see Sect. 3.2), for which the difference in the overall maximum is much larger (factor ≈ 2).

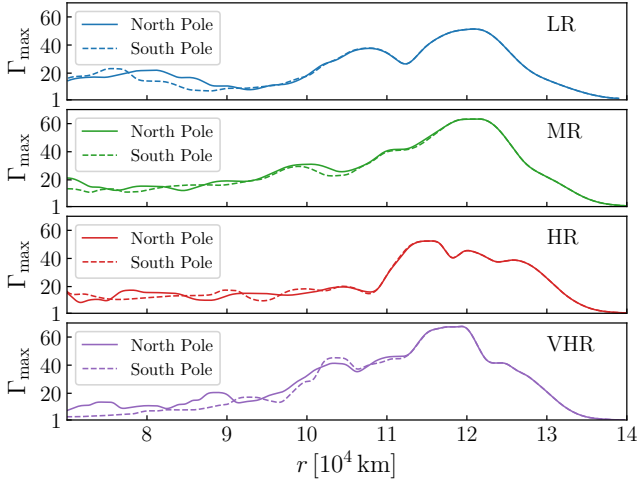


Figure C1. Radial profiles of maximum Lorentz factor at 572 ms after merger (maximum value achieved at each radial distance). North and south profiles are shown for the four different resolutions (top to bottom): LR, MR, HR and VHR (see text for details).

For the purposes of the present work, the effects due to the mismatch in the initial internal energy are acceptable. On the other hand, a fully consistent EOS would eliminate such a potential source of error. This could be obtained by adapting the EOS employed in the BNS merger simulation so that it reproduces the Taub EOS below rest-mass densities of 10^8 g/cm^3 .

APPENDIX C: RESOLUTION STUDY

To evaluate how our results depend on resolution, we performed simulations of our fiducial model (Sect. 3.1) with four different settings:

- Low Resolution (LR): $540 \times 180 \times 360$ points along r , θ , and ϕ , respectively ;
- Medium Resolution (MR): $648 \times 216 \times 432$ points ;
- High Resolution (HR): $756 \times 252 \times 504$ points ;
- Very High Resolution (VHR): $864 \times 288 \times 576$ points ,

where HR is our fiducial resolution. Below, we compare the outcome at 572 ms after merger. In particular, we focus on the Lorentz factor distribution at that time.

In Fig. C1 we report the radial profile of the maximum Lorentz factor computed for the different resolutions (increasing from top to bottom). In Fig. C2, we show the meridional view of the Lorentz factor, zooming in the region of the jet’s head (north side only), with resolution increasing from left to right. From both Figures, we can appreciate the gradual appearance of finer spatial modulations as the resolution increases. Significant differences are still present between the two highest resolutions, i.e. HR and VHR, which indicates that we are not yet in a regime of convergence. While a precise assessment of numerical errors is beyond our present scope, future studies presenting quantitative results will thus require higher resolutions (corresponding to our VHR or higher).

APPENDIX D: EXTRAPOLATION TEST

We present here the results of a PLUTO simulation where we import data from the BNS merger simulation at 141 ms after merger

and evolve the system up to 156 ms with the prescriptions given in Section 2.2 (with no collapse to a BH nor jet injection). To specify the additional acceleration accounting for radial pressure gradients, we adopt the effective mass at the excision radius and its time evolution as given by the exponential fit shown in Figure 10. Our aim is to test the reliability of such an evolution by comparing the system properties at 156 ms with those given by the BNS merger simulation itself.

Figure D1 shows the radial profiles of the angle-averaged radial velocities at 141 and 156 ms, for both the test PLUTO simulation and the original BNS merger simulation. Starting from the very same profile at 141 ms, the PLUTO simulation with the chosen prescriptions is able to reproduce almost exactly the final profile at 156 ms, with only a slight discrepancy close to the excision radius (below 500 km).

In the same Figure, we also report the result obtained by retaining only 10% of the contribution of external forces (i.e. gravitational pull and additional acceleration related to radial pressure gradients). The large discrepancy demonstrates how the external forces contribution is fundamental to reproduce the correct behaviour.⁷

In Figure D2, we show the rest-mass density in the meridional xy -plane at 156 ms for the two cases. The correspondence is very good in the inner and denser region up to $\approx 1000 \text{ km}$ radius, where also the lower density funnel along the y -axis is preserved. At larger distances, we notice that the surrounding cloud of material is slightly more expanded in the PLUTO case.

In conclusion, the test shows that our prescription to continue or extrapolate the post-merger evolution in PLUTO gives, at least in this phase ($\sim 150 \text{ ms}$ after merger), a rather good agreement with what is obtained in the actual BNS merger simulation and therefore it represents a viable compromise between simplicity and physical accuracy.

This paper has been typeset from a \LaTeX file prepared by the author.

⁷ We also note that, in this phase of the evolution, removing entirely the external forces would even cause the simulation to fail.

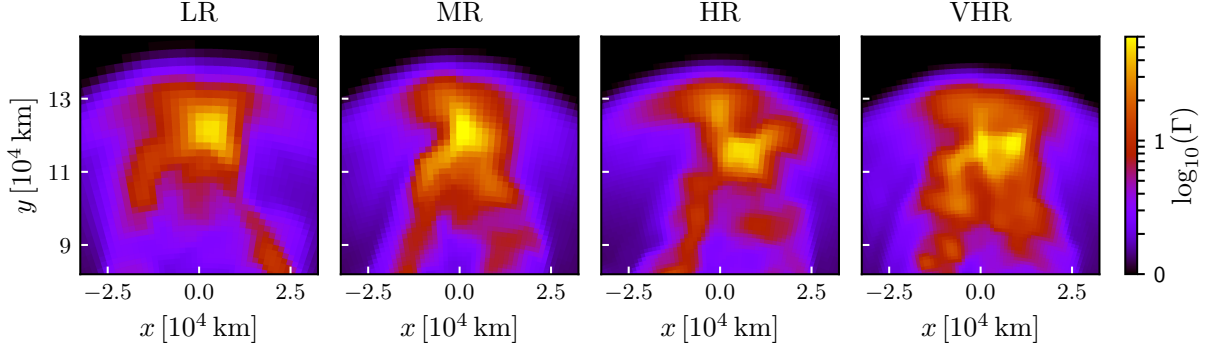


Figure C2. Meridional view of the Lorentz factor at the jet's head (north side only) computed at 572 ms after merger. The four panels show the results at four different resolutions (left to right): LR, MR, HR and VHR (see text for details).

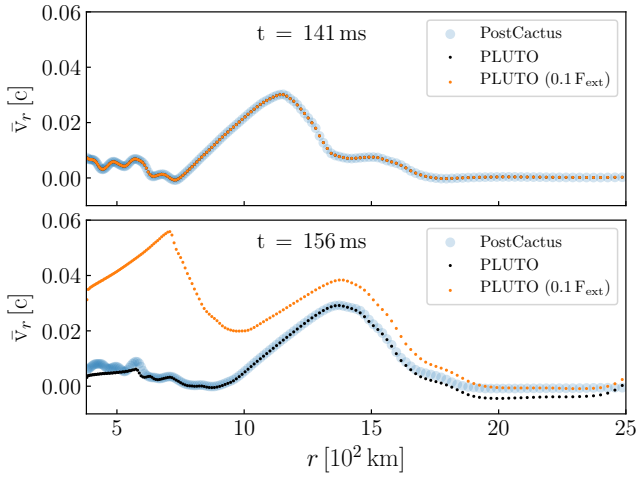


Figure D1. Radial profiles of the angle-averaged radial velocity at 141 ms and 156 ms after merger (upper and lower panels, respectively). The blue dots are obtained by importing data from our reference BNS merger simulation at the given time (Section 2.1). The black dots correspond instead to the result of our test PLUTO simulation, which starts from the same initial data at 141 ms and then evolves the system according to the adopted prescriptions (see text for details). Finally, the orange dots correspond to the same PLUTO simulation where we only retain 10% of the contribution of external forces.

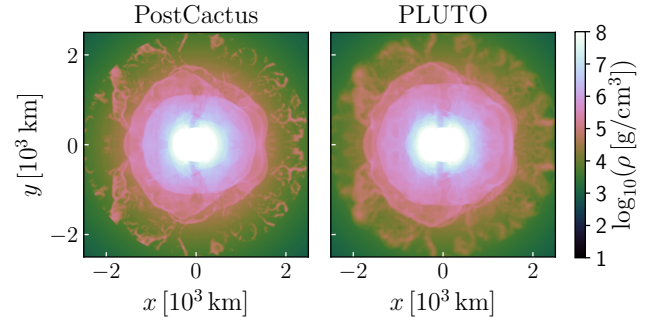


Figure D2. Meridional view of the rest-mass density at 156 ms after merger for the same two cases shown in Figure D1, i.e. data imported from our reference BNS merger simulation (left) and the result of the evolution in PLUTO starting from data imported at 141 ms (right). The white circle of 380 km radius corresponds to the excised region (as in Figs. 1 and 3).